

Title	Origin of the visible-light response of nickel(II) oxide cluster surface modified titanium(IV) dioxide
Authors	Iwaszuk, Anna;Nolan, Michael;Jin, Qiliang;Fujishima, Musashi;Tada, Hiroaki
Publication date	2013-01-24
Original Citation	Iwaszuk, A., Nolan, M., Jin, Q., Fujishima, M. and Tada, H. (2013) 'Origin of the Visible-Light Response of Nickel(II) Oxide Cluster Surface Modified Titanium(IV) Dioxide', The Journal of Physical Chemistry C, 117(6), pp. 2709-2718. doi: 10.1021/jp306793r
Type of publication	Article (peer-reviewed)
Link to publisher's version	<a href="http://pubs.acs.org/doi/abs/10.1021/jp306793r">http://pubs.acs.org/doi/abs/10.1021/jp306793r</a> - 10.1021/jp306793r
Rights	© 2013 American Chemical Society. This document is the Accepted Manuscript version of a Published Work that appeared in final form in The Journal of Physical Chemistry C, copyright © American Chemical Society after peer review and technical editing by the publisher. To access the final edited and published work see <a href="http://pubs.acs.org/doi/abs/10.1021/jp306793r">http://pubs.acs.org/doi/abs/10.1021/jp306793r</a>
Download date	2025-04-18 04:31:45
Item downloaded from	<a href="https://hdl.handle.net/10468/1595">https://hdl.handle.net/10468/1595</a>



# UCC

**University College Cork, Ireland**  
Coláiste na hOllscoile Corcaigh

# Origin of the Visible-Light Response of Nickel(II) Oxide Cluster Surface Modified Titanium(IV) Dioxide

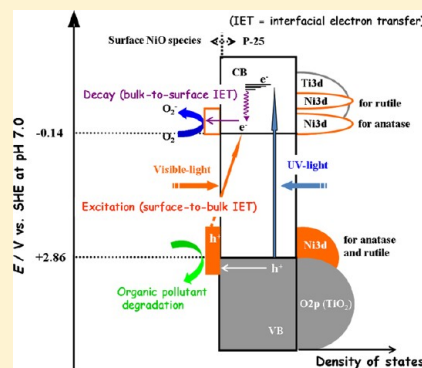
Anna Iwazuk,<sup>†</sup> Michael Nolan,<sup>\*,†</sup> Qiliang Jin,<sup>‡</sup> Musashi Fujishima,<sup>‡</sup> and Hiroaki Tada<sup>\*,‡</sup>

<sup>†</sup>Tyndall National Institute, University College Cork, Lee Maltings, Prospect Row, Cork, Ireland

<sup>‡</sup>Department of Applied Chemistry, School of Science and Engineering, Kinki University, 3-4-1, Kowakae, Higashi-Osaka, Osaka 577-8502, Japan

**S** Supporting Information

**ABSTRACT:** A number of NiO clusters have been formed on TiO<sub>2</sub> (anatase/rutile = 4/1 w/w, P-25, Degussa) in a highly dispersed state (NiO/TiO<sub>2</sub>) by the chemisorption–calcination cycle technique. The NiO/TiO<sub>2</sub> causes high visible-light activities for the degradations of 2-naphthol and *p*-cresol exceeding those of FeO<sub>x</sub>/TiO<sub>2</sub> (Tada et al. *Angew. Chem., Int. Ed.* **2011**, *50*, 3501–3505). The main purpose of this study is to clarify the origin at an electronic level by the density functional simulation for NiO, Ni<sub>2</sub>O<sub>3</sub>, and Ni<sub>4</sub>O<sub>4</sub> clusters supported on TiO<sub>2</sub> rutile (110) and anatase (001) surfaces. The clusters adsorb strongly on both rutile and anatase with adsorption energies ranging from –3.18 to –6.15 eV, creating new interfacial bonds between the clusters and both surfaces. On rutile, intermetallic Ni–Ti bonds facilitate stronger binding compared with anatase. The electronic structure shows that the top of the valence bands (VBs) of rutile and anatase arises from electronic states on the NiO cluster. On the other hand, the conduction band of rutile is from the Ti 3d states, whereas NiO cluster levels are generated near the conduction band minimum of anatase. This is in contrast to the SnO<sub>2</sub>/rutile TiO<sub>2</sub> system, where the density of states near the conduction band minimum increases with the VB unmodified. In the NiO/TiO<sub>2</sub> system, the band gaps of both rutile and anatase are narrowed by up to 0.8 eV compared with pristine TiO<sub>2</sub>, which pushes the photoactivity into the visible region. In view of the calculated electronic structure, we have attributed the enhanced photocatalytic activity both to the charge separation due to the excitation from the Ni 3d surface sub-band to the TiO<sub>2</sub> conduction band and the action of the NiO species as a mediator for the electron transfer from the TiO<sub>2</sub> conduction band to O<sub>2</sub>.



## 1. INTRODUCTION

One of the biggest challenges for our energy security is to be independent of fossil fuels, and the development of suitable photocatalysts may help in solar energy harvesting. TiO<sub>2</sub> has gathered much attention because it is relatively cheap, readily available, stable, and nontoxic. Since TiO<sub>2</sub> absorbs only in the ultraviolet region, there have been many attempts to modify it in such a way that it will also absorb visible light.<sup>1,2</sup> A popular approach for material modification over many years has been substitutional cation or anion doping at titanium or oxygen sites.<sup>3–19</sup> In 2001, Asahi et al. demonstrated that N-doping of TiO<sub>2</sub> results in visible light absorption,<sup>3</sup> and there has been much work since devoted to examining doping as a means to shifting the band gap of TiO<sub>2</sub> from the UV to the visible. N-doped TiO<sub>2</sub> continues to be of great interest and has been studied in depth by Di Valentin, Pacchioni, and Selloni in refs 4 and 5, while there have been recent experimental and modeling reports on this prototype of doped TiO<sub>2</sub>.<sup>6,7</sup> Carbon-doped TiO<sub>2</sub> has also been of great interest,<sup>8–11</sup> while Wang and Lewis have used the FIREBALL code to study doping of TiO<sub>2</sub><sup>12,13</sup> and obtained results that were used to explain the band gap changes in doped TiO<sub>2</sub>. Finally, other studies of doped TiO<sub>2</sub> in

refs 14–19 serve to highlight the range of dopants that have been studied.

It has been highlighted that there are practical questions associated with doping of TiO<sub>2</sub>, including solubility, stability, determining that doping has actually taken place, and charge recombination.<sup>20,21</sup> Herrmann has shown that Cr-doping of TiO<sub>2</sub>, which does reduce the band gap, will in fact have a detrimental effect on the photocatalytic activity.<sup>22</sup> With this in mind, there have been many efforts to find alternative ways to shift the band gap of TiO<sub>2</sub> in order to make it more efficient in terms of visible-light absorption and reducing charge recombination. This includes modification with metal particles, such as gold,<sup>21</sup> modification with quantum dots, for example, CdS<sup>23</sup> (which, although displaying an initially high photocatalytic efficiency, does subsequently degrade as a result of CdS oxidation), and heterostructures of graphene and TiO<sub>2</sub>.<sup>24</sup>

Recent studies have demonstrated that oxide–oxide heterostructures composed of nanoscale metal oxide clusters on TiO<sub>2</sub> can drastically improve the photocatalytic properties

Received: July 9, 2012

Revised: January 23, 2013

68 compared to pure  $\text{TiO}_2$ .<sup>25–31</sup> Modification of  $\text{TiO}_2$  with metal  
69 oxide nanoclusters has been investigated by Libera et al.<sup>29</sup> and  
70 Tada et al.<sup>30,31</sup> Libera et al. used the atomic layer deposition  
71 technique to deposit  $\text{Fe}_2\text{O}_3$  nanoclusters on  $\text{TiO}_2$  and found  
72 visible-light absorption and efficient photocatalytic degradation  
73 of methylene blue.<sup>29</sup> Tada et al. synthesized  $\text{FeO}_x$ -modified  
74  $\text{TiO}_2$  using the chemisorption–calcination cycle (CCC) that  
75 deposits highly dispersed metal oxide nanoclusters on the  $\text{TiO}_2$   
76 surface at a molecular scale.<sup>30</sup> The  $\text{FeO}_x/\text{TiO}_2$  structure shows  
77 improved visible-light activity and also good UV-light activity.  
78 These features came from band gap narrowing and were  
79 explained by the presence of the  $\text{FeO}_x$  clusters that are  
80 responsible for shifting the valence band (VB) maximum of  
81  $\text{TiO}_2$ .<sup>31</sup> Further, with  $\text{SnO}_2$ -modified  $\text{TiO}_2$ , striking differences  
82 between the light absorption properties and the visible-light  
83 photocatalytic activity of modified rutile and anatase  $\text{TiO}_2$  were  
84 observed and rationalized with first-principles simula-  
85 tions.<sup>32,33</sup> Other examples of heterostructures have included  
86  $\text{BiOBr-ZnFe}_2\text{O}_4$ ,<sup>27</sup>  $\text{BiVO}_4\text{-WO}_3$ ,<sup>28</sup>  $\text{SnO}_x\text{-ZnGa}_2\text{O}_4$ ,<sup>34</sup> and  
87  $\text{AgI-BiO}$ ,<sup>35</sup> displaying improved photocatalytic activity com-  
88 pared to the pure oxides or simple physical mixtures,  
89 highlighting the important role of the interface.<sup>35</sup> Further, the  
90  $\text{Ni}^{2+}$  surface modification of rutile  $\text{TiO}_2$  by the impregnation  
91 method was reported to enhance both the UV- and visible-light  
92 activities, whereas the effect is much smaller than that by the  
93  $\text{Fe}^{3+}$  surface modification.<sup>36</sup> Recently, we have shown that the  
94 surface modification of  $\text{TiO}_2$  with extremely small NiO clusters  
95 by the CCC technique ( $\text{NiO}/\text{TiO}_2$ ) causes a high visible-light  
96 activity concomitantly with the UV-light activity increased for  
97 the decomposition of 2-naphthol.<sup>37</sup> However, the origin of the  
98 visible-light response is not fully understood and needs further  
99 investigation to facilitate the development of this exciting  
100 approach to developing photocatalytic materials.

101 On the other hand, to understand the origin of the  
102 experimental findings, density functional theory (DFT)  
103 simulations are of great help. Iwaszuk and Nolan have shown  
104 that that subnanometer diameter ( $\text{TiO}_2$ )<sub>*n*</sub> clusters, with *n* = 2–  
105 4, adsorbed on the rutile  $\text{TiO}_2(110)$  surface, can reduce the  
106 band gap compared to pure  $\text{TiO}_2$  (although that work was also  
107 focused on examining the reactivity of these heterostruc-  
108 tures).<sup>38</sup> The presence of Ti 3d states of the cluster above the  
109 VB will enhance charge separation, and the photocatalytic  
110 activities will be improved.<sup>38</sup> Moreover, further work has  
111 demonstrated that modification of  $\text{TiO}_2$  with other transition  
112 metal oxides will also result in potentially useful photocatalytic  
113 properties. For example, DFT simulations show that small  
114 transition metal oxide nanoclusters, for example,  $\text{Cr}_2\text{O}_3$  and  
115  $\text{Mo}_2\text{O}_4$ , deposited on  $\text{TiO}_2$  rutile (110) will lead to a band gap  
116 reduction<sup>39</sup> and improvement of photocatalytic activities. Thus,  
117 the surface modification of the catalyst is an approach that may  
118 benefit over doping by reducing formation of localized  
119 electronic states and electron/hole recombination that are the  
120 key factors for an efficient photocatalyst.

121 Herein, we report that  $\text{NiO}/\text{TiO}_2$  (anatase/rutile = 4/1 w/w,  
122 specific surface area =  $50 \text{ m}^2 \text{ g}^{-1}$ , P-25, Degussa) exhibits high  
123 levels of visible-light activities for 2-naphthol and *p*-cresol  
124 degradations concurrently with enhanced UV-light activity. P-  
125 25 possesses high UV-light activity for the degradation of most  
126 organic compounds. Furthermore, in elucidating the origin of  
127 the activity of  $\text{NiO}$ -modified  $\text{TiO}_2$ , we show by spectroscopic  
128 measurements and DFT calculations that the visible-light  
129 response of modified  $\text{TiO}_2$  is induced by the rise in the VB top  
130 with  $\text{NiO}$  surface modification. We investigate the  $\text{TiO}_2$  anatase

(001) and rutile (110) surfaces modified with  $\text{NiO}$  nanoclusters 131  
using DFT simulations to establish (1) how  $\text{NiO}$  nanocluster 132  
modification of  $\text{TiO}_2$  changes the light absorption properties 133  
and (2) if there is any sensitivity to  $\text{TiO}_2$  crystal form, as 134  
observed for  $\text{SnO}_2$ .<sup>33</sup> We investigated representative structures 135  
of  $\text{NiO}$ ,  $\text{Ni}_2\text{O}_3$ , and  $\text{Ni}_4\text{O}_4$  nanoclusters deposited on both 136  
 $\text{TiO}_2$  surfaces. All  $\text{NiO}$  clusters adsorb strongly on both 137  
surfaces; however, adsorption is stronger at the rutile (110) 138  
surface due to formation of additional Ni–Ti metallic bonds 139  
that are not possible at the anatase (001) surface. The 140  
electronic structure shows that the band gap is narrowed and 141  
the energy band alignments will give electron and hole 142  
separation after light excitation. 143

## 2. METHODOLOGY

**2.1. Photocatalyst Synthesis.** The  $\text{NiO}/\text{P-25}$  was 144  
prepared by the CCC technique.<sup>30</sup> After P-25 (1 g) had been 145  
added to 100 mL of a  $\text{Ni}(\text{acac})_2(\text{H}_2\text{O})_2$  solution (solvent, 146  
ethanol/*n*-hexane = 3:17 v/v), they were allowed to stand for 147  
24 h at 298 K. The  $\text{Ni}(\text{acac})_2(\text{H}_2\text{O})_2$  concentration was 148  
changed ranging from  $1 \times 10^{-5}$  to  $\sim 5 \times 10^{-3}$  M. The resulting 149  
samples were washed repeatedly with the solvent for the 150  
physisorbed complexes to be removed and dried, followed by 151  
heating in air at 773 K for 1 h. The complex adsorption and the 152  
subsequent heating were repeated to increase the Ni loading 153  
amount. The loading amount was shown by the amount of Ni 154  
loaded on the unit surface area of P-25 ( $\Gamma$ , ions  $\text{nm}^{-2}$ ). 155

**2.2. Photocatalyst Characterization.** High-resolution 156  
transmission electron microscopy (HRTEM) observation and 157  
X-ray energy dispersive spectroscopic measurements were 158  
performed using a JEOL JEM-3000F and a Gatan imaging 159  
filter at an applied voltage of 300 or 297 kV. UV–visible diffuse 160  
reflectance spectra of  $\text{NiO}/\text{TiO}_2$  were recorded on a Hitachi U- 161  
4000 spectrophotometer. The spectra were converted to the 162  
absorption spectra by using the Kubelka–Munk function. X-ray 163  
photoelectron spectroscopic (XPS) measurements were 164  
performed using a Kratos Axis Nova X-ray photoelectron 165  
spectrometer with a monochromated Al  $K\alpha$  X-ray source ( $h\nu =$  166  
1486.6 eV) operated at 15 kV and 10 mA. The takeoff angle 167  
was  $90^\circ$ , and multiplex spectra were obtained for Ni 2p, O 1s, 168  
and Ti 2p photopeaks. All the binding energies were referenced 169  
with respect to the C 1s at 284.6 eV. The photoluminescence 170  
spectra were measured with an excitation wavelength of 320 nm 171  
at 77 K using a JASCO FP-6000 spectrofluorometer. 172

**2.3. Photocatalytic Reactions.** A 50 mL amount of  $1.0 \times$  173  
 $10^{-5}$  M 2-naphthol solution (solvent, acetonitrile/water = 1:99 174  
v/v) or  $5.0 \times 10^{-4}$  M *p*-cresol solution (solvent, water) was 175  
placed in a double-jacket-type reaction cell made of borosilicate 176  
glass, and then, P-25 (Degussa) or  $\text{NiO}/\text{P-25}$  particles (0.1 g) 177  
were added. The reaction cell was irradiated with a Xe lamp 178  
(Wacom XRD-501SW) through a band-pass filter (33U, 179  
SIGMA KOKI CO., Ltd.) superposed on FTO-coated glass 180  
(two pieces of FTO glass for 2-naphthol and a piece of FTO 181  
glass for *p*-cresol) transmitting only the 330–400 nm range for 182  
the UV-light photocatalytic activity evaluation and a high-pass 183  
filter (L-42, Toshiba) to cut off UV light for the visible-light- 184  
induced activity test. The irradiation conditions are as follows: 185  
for 2-naphthol UV light,  $330 < \lambda < 400 \text{ nm}$ ,  $I_{320-400 \text{ nm}} = 0.5$  186  
 $\text{mW cm}^{-2}$ , and visible light,  $\lambda > 400 \text{ nm}$ ,  $I_{420-485 \text{ nm}} = 1.0$  187  
 $\text{mW cm}^{-2}$ ; for *p*-cresol UV light,  $330 < \lambda < 400 \text{ nm}$ ,  $I_{320-400 \text{ nm}} = 2$  188  
 $\text{mW cm}^{-2}$ , and visible light,  $\lambda > 400 \text{ nm}$ ,  $I_{420-485 \text{ nm}} = 2$  189  
 $\text{mW cm}^{-2}$ . A 3 mL amount of the solution was sampled every 15 190  
min, and the absorbance at  $\lambda = 224 \text{ nm}$  was measured using a 191

192 spectrometer (UV-1800, Shimadzu) to determine the concen-  
193 tration of 2-naphthol. The *p*-cresol concentration was  
194 determined by high-performance liquid chromatography  
195 (SPD-6A, Shimadzu; column = Fluofix INW425 4.6 mm ×  
196 250 mm (NEOS); mobile phase = water–ethanol (3:7 v/v); λ  
197 = 277 nm).

198 **2.4. DFT Simulation.** For modeling TiO<sub>2</sub> rutile (110) and  
199 anatase (001) surfaces, we use three-dimensional periodic slab  
200 models with the VASP code.<sup>40</sup> The valence electrons are  
201 described by a plane wave basis set, and the cutoff for kinetic  
202 energy is 396 eV. The valence electrons are 4 for Ti, 6 for O,  
203 and 10 for Ni, within the PAW approximation, and the  
204 exchange–correlation functional is the approximation of  
205 Perdew–Wang (PW91).<sup>41,42</sup> The Monkhorst–Pack scheme is  
206 used for k-point sampling with a (2 × 2 × 1) sampling grid.  
207 The rutile (110) surface is terminated by 2-fold coordinated  
208 bridging oxygen atoms, and the next sublayer consists of 6-fold  
209 and 5-fold coordinated Ti atoms. The (unreconstructed) (001)  
210 surface model of anatase is terminated by 2-fold coordinated  
211 oxygen and has 5-fold coordinated Ti ions in the next sublayer.  
212 We use models of rutile (110) and anatase (001), since (110) is  
213 by far the most stable surface of rutile and is well studied,<sup>43</sup>  
214 while for anatase, (001) is of great interest as the most  
215 photocatalytically active anatase surface.<sup>44,45</sup> We consider the  
216 rutile and anatase surfaces in their perfect, stoichiometric form,  
217 with consideration of the OH-terminated surfaces that are well  
218 known for TiO<sub>2</sub> being the subject of ongoing studies. In order  
219 to have isolated NiO nanoclusters, we employed a (2 × 4)  
220 surface supercell for each TiO<sub>2</sub> surface; for the largest NiO  
221 nanocluster considered, a (4 × 4) rutile (110) surface was also  
222 studied to examine the effect of the interaction of NiO clusters  
223 with periodic images on the resulting properties, with the larger  
224 surface supercell giving a bigger distance between periodic NiO  
225 images, thus reducing the periodic interactions and modeling  
226 more widely separated NiO nanoclusters. NiO nanoclusters  
227 with composition NiO, Ni<sub>2</sub>O<sub>2</sub>, Ni<sub>3</sub>O<sub>3</sub>, and Ni<sub>4</sub>O<sub>4</sub> are studied as  
228 representative molecular-sized NiO nanoclusters. The super-  
229 cells and technical parameters for the free nanoclusters are the  
230 same as the extended surfaces.

231 For the calculations we use the DFT+*U* approach<sup>46,47</sup> where  
232 we applied *U* = 4.5 eV on the Ti 3d states. The need to  
233 introduce the *U* parameter in order to describe properly  
234 electronic states of d or f shells is well known.<sup>46–50</sup> We also  
235 applied the +*U* correction for Ni in NiO, since the electronic  
236 states of NiO are known to be poorly described with  
237 DFT;<sup>46,47,51–53</sup> for Ni, we apply *U* = 8 eV and *J* = 1 eV (giving  
238 *U* – *J* = 7 eV), generally consistent with values from the  
239 literature, for example, refs 51–53; a check with other values of  
240 *U*, namely, (*U* – *J*) = 5 and 6 eV, gives similar results to those  
241 found here for the electronic structure. The DFT+*U* approach  
242 gives a reasonable description of transition metal d states, but  
243 still an underestimation of band gap remains, and this depends  
244 on the precise DFT+*U* setup. With this in mind, the change in  
245 the band gap of TiO<sub>2</sub> upon modification with NiO, which is  
246 more reliable, is our primary focus.

247 The clusters were deposited on both TiO<sub>2</sub> surfaces and fully  
248 relaxed. The adsorption energy was computed from the  
249 following:

$$E^{\text{ads}} = E((\text{NiO})_n - \text{TiO}_2) - \{E((\text{NiO})_n) + E(\text{TiO}_2)\} \quad (1)$$

251 where  $E((\text{NiO})_n - \text{TiO}_2)$  is the total energy of the NiO  
252 nanocluster supported on the surface and  $E((\text{NiO})_n)$  and

$E(\text{TiO}_2)$  are the total energies of the free cluster and the bare  
253 surface, respectively. A negative adsorption energy signifies that  
254 the cluster adsorption is stable. 255

### 3. RESULTS

The point of effective surface modification of TiO<sub>2</sub> with metal  
256 oxide clusters is the dispersion state and the strict control of the  
257 loading amount.<sup>30</sup> The Ni(acac)<sub>2</sub>(H<sub>2</sub>O)<sub>2</sub> complex is chem-  
258 isorbed on P-25 via the partial ligand exchange between the  
259 acac ligand and the acidic surface Ti–OH group to yield NiO  
260 clusters by postheating.<sup>37</sup> Figure 1 shows HRTEM micrographs  
261 of

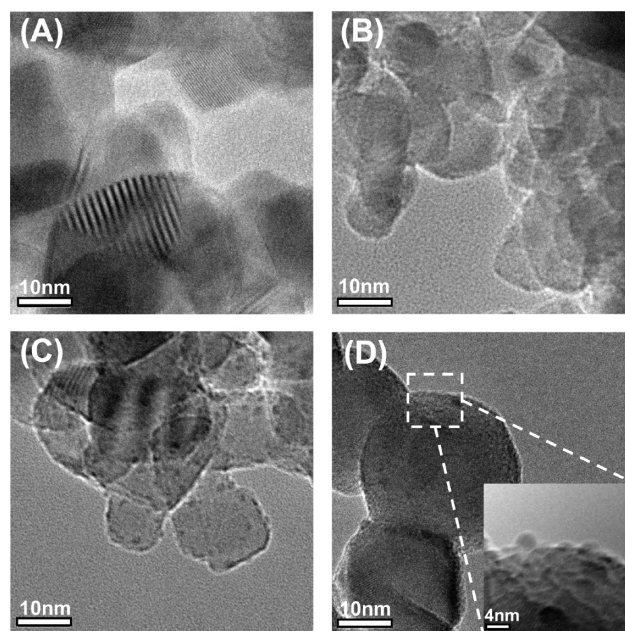


**Figure 1.** HRTEM images of NiO/P-25: (A)  $\Gamma = 0$ ; (B)  $\Gamma = 0.014$ ;  
(C)  $\Gamma = 0.47$ ; (D)  $\Gamma = 0.83$ .

of NiO/TiO<sub>2</sub> with varying Ni loading amount  $\Gamma$  (ions nm<sup>-2</sup>).  
262 Highly dispersed NiO clusters smaller than ~2 nm are observed  
263 on the surface of P-25. The strong chemisorption of the  
264 complex on the TiO<sub>2</sub> surface (DFT results) prevents  
265 aggregation of the small NiO clusters into larger structures  
266 during the subsequent heating, thus yielding extremely small  
267 adsorbed NiO clusters. 268

2-Naphthol and *p*-cresol were used as model water  
269 pollutants. 2-Naphthol, a starting material of azo-dyes, has no  
270 absorption at  $\lambda > 330$  nm.<sup>54</sup> Both the degradations of 2-  
271 naphthol and *p*-cresol apparently followed the first-order rate  
272 law under irradiation of UV light and visible light, and the  
273 activity was evaluated by the pseudofirst-order rate constant (*k*,  
274 h<sup>-1</sup>). Figure 2A (red circles) shows visible-light activity for the  
275 2-naphthol degradation as a function of  $\Gamma$ . The surface  
276 modification with NiO clusters endows P-25 with visible-light  
277 activity, whereas pristine P-25 has only low activity. The visible-  
278 light activity drastically increases with increasing  $\Gamma$ , passing  
279 through a maximum at  $\Gamma \sim 0.32$ . The maximum activities of  
280 several metal oxide surface modified P-25 are on the order of  
281 NiO > FeO<sub>x</sub> > SnO<sub>2</sub> > none under the same reaction  
282 conditions, and the value of NiO/P25 reaches approximately  
283 twice that of the FeO<sub>x</sub>/P-25 system (Table S1, Supporting  
284 Information).<sup>30</sup> Figure 2B (red circles) shows UV-light activity  
285 for the 2-naphthol degradation as a function of  $\Gamma$ . The UV-light  
286 activity further increases by the surface modification with the  
287

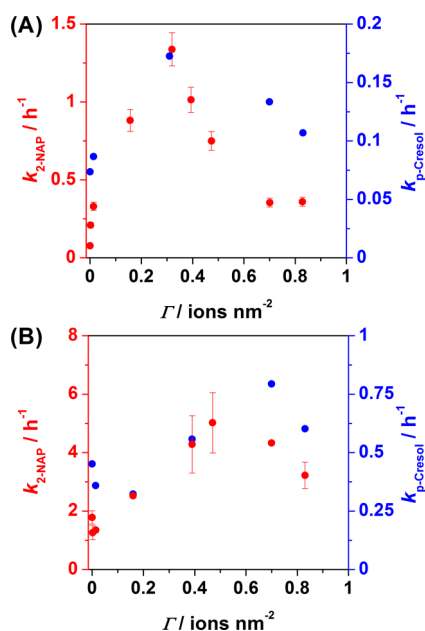


**Figure 2.** (A) Visible-light and (B) UV-light activities of NiO/P-25 for 2-naphthol (red circles) and *p*-cresol (blue circles) degradations.

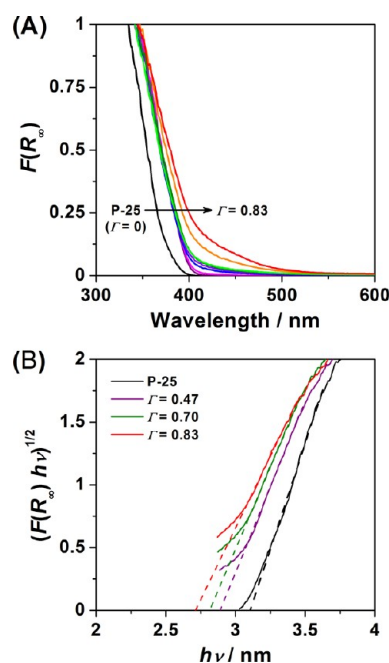


**Figure 3.** (A) UV–visible absorption spectra of NiO/P-25 with varying  $\Gamma$ :  $F(R_\infty)$  denotes the Kubelka–Munk function. (B) Plots of  $(F(R_\infty)h\nu)^{1/2}$  vs  $h\nu$ .

288 NiO clusters. The loading at  $\Gamma = 0.47$  affords a maximum  
 289 activity, which is  $\sim 2.8$  times the activity of P-25. The maximum  
 290 activities of several metal oxide surface modified P-25 are on  
 291 the order of  $\text{FeO}_x > \text{NiO} > \text{SnO}_2 \sim \text{none}$  (Table S1,  
 292 Supporting Information). We have recently reviewed the  
 293 difference in the surface modification effect between  $\text{FeO}_x$   
 294 and  $\text{SnO}_2$  clusters.<sup>55</sup> On the other hand, *p*-cresol widely used as  
 295 a sterilizer and disinfectant has no absorption at  $\lambda > 330$  nm. As  
 296 shown in Figure 2A,B (blue circles), similar trends are also  
 297 observed for the degradation of *p*-cresol, while the enhance-  
 298 ment effect is somewhat smaller as compared to that for the 2-  
 299 naphthol degradation.

300 The effect of the surface modification of P-25 with varying  
 301 amounts of NiO clusters on the optical property was studied.  
 302 Ni-doped  $\text{TiO}_2$  prepared by the solid-state reaction of  $\text{TiO}_2$   
 303 with NiO has a broad and weak absorption around 450 nm due  
 304 to the d–d transition, while the intrinsic absorption edge is  
 305 invariant.<sup>56</sup> Chemical doping of Cr and N ions into  $\text{TiO}_2$  yields  
 306 similar weak shoulders in the visible region due to the  
 307 formation of localized impurity levels within the band gap.<sup>57</sup>

308 Figure 3A shows UV–visible absorption spectra of NiO/P-  
 309 25 with varying  $\Gamma$ :  $F(R_\infty)$  is the Kubelka–Munk function. In  
 310 contrast to the spectra of Ni-doped  $\text{TiO}_2$ , band gap narrowing  
 311 occurs for NiO/P-25, whereas the d–d transition band grows at

312  $\Gamma > 0.47$ . Figure 3B shows plots of  $[F(R_\infty)h\nu]^{1/2}$  versus  $h\nu$  for  
 313 NiO/P-25.<sup>58</sup> The indirect band gap determined from the  
 314 extrapolation of the tangent to the abscissa decreases from 3.1  
 315 eV at  $\Gamma = 0$  to 2.6 eV at  $\Gamma = 0.83$ . A similar spectral feature is  
 316 observed for Cr-<sup>59</sup> and N-doped<sup>60</sup>  $\text{TiO}_2$  prepared by physical  
 317 techniques such as ion implantation and magnetron sputtering.  
 318 Also, the VB-XPS was measured for NiO/P-25 with varying  $\Gamma$ .  
 319 As shown in Figure 4A, the emission from the VB extends from  
 320 2 to 9 eV for every sample. Figure 4B magnifies the energy  
 321 region near the VB maximum. The top of the VB rises with an  
 322 increase in  $\Gamma$ . The magnitude of the change reaches  
 323 approximately 0.5 eV at  $\Gamma = 0.83$ , which is comparable with  
 324 the decrement in the band gap with the surface modification.  
 325 Consequently, the visible-light absorption of  $\text{TiO}_2$  by the

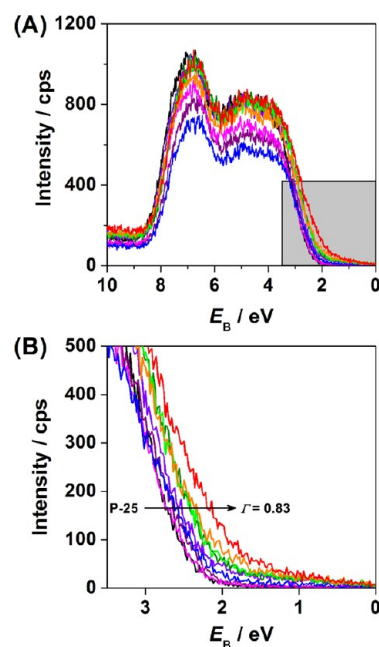


**Figure 4.** (A) VB-XPS of NiO/P-25 ( $\Gamma = 0, 0.0018, 0.014, 0.16, 0.32, 0.39, 0.47, 0.70,$  and  $0.83$  from left to right). (B) Magnified VB-XPS near the VB maximum.

surface modification with the NiO clusters stems from the rise  
 in the top of the VB.

To understand the effect of the surface modification with the  
 NiO clusters at an electronic level, DFT simulations were  
 performed for model systems consisting of  $\text{TiO}_2$  and NiO  
 nanoclusters adsorbed at rutile and anatase. Figure 5 presents  
 the atomic structure of the NiO,  $\text{Ni}_2\text{O}_2$ ,  $\text{Ni}_3\text{O}_3$ , and  $\text{Ni}_4\text{O}_4$   
 nanoclusters, which are chosen as representative NiO nano-  
 clusters, adsorbed on  $\text{TiO}_2$  anatase (001) and rutile (110)  
 surfaces together with the adsorption energies and the

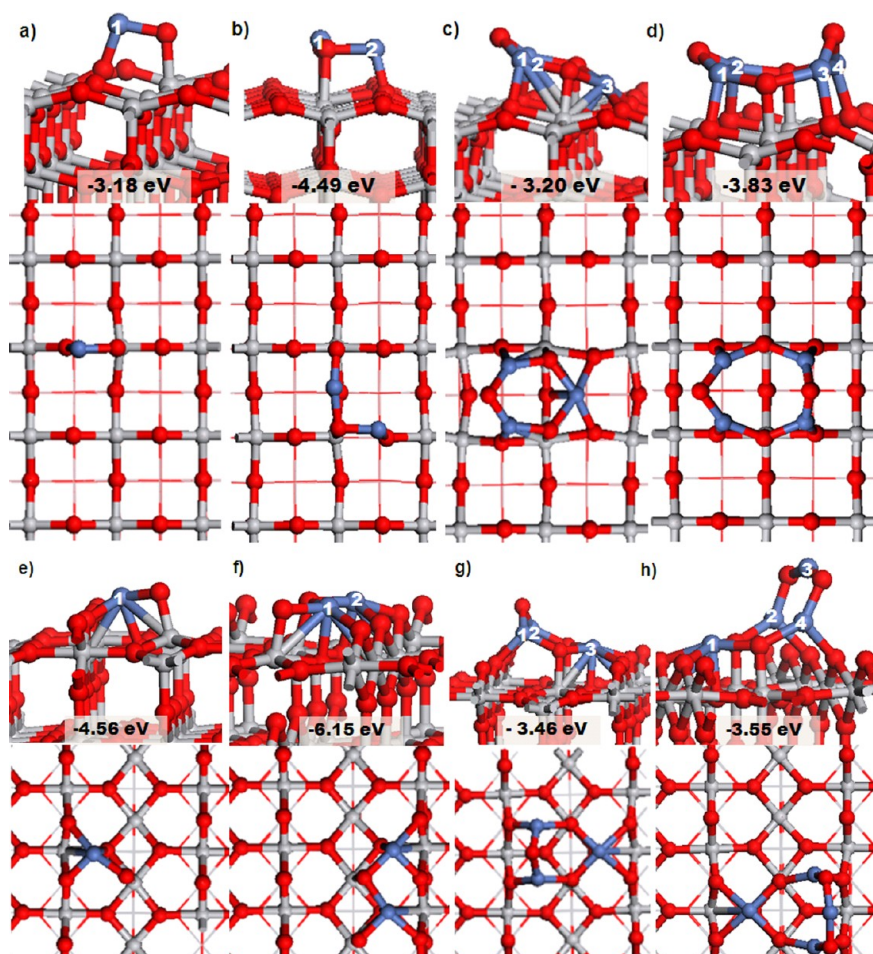


**Figure 5.** Relaxed adsorption structures with adsorption energies given in eV for (a) NiO, (b) Ni<sub>2</sub>O<sub>2</sub>, (c) Ni<sub>3</sub>O<sub>3</sub>, and (d) Ni<sub>4</sub>O<sub>4</sub> clusters on TiO<sub>2</sub> anatase (001) and (e) NiO, (f) Ni<sub>2</sub>O<sub>2</sub>, and (g) Ni<sub>3</sub>O<sub>3</sub> clusters on TiO<sub>2</sub> rutile (110). The blue spheres are Ni atoms, the gray spheres are Ti atoms, and the red spheres are O atoms. Cluster Ni atoms are numbered.

336 numbering of the nanocluster Ni atoms. We compute the  
 337 coverage of the nanoclusters in terms of Ni atoms per unit area,  
 338 so that for NiO, Ni<sub>2</sub>O<sub>2</sub>, Ni<sub>3</sub>O<sub>3</sub>, and Ni<sub>4</sub>O<sub>4</sub> on anatase (001), the  
 339 coverages are 0.85, 1.70, 2.55, and 3.41 Ni atoms/nm<sup>2</sup>. On  
 340 rutile (110), the corresponding coverages are 0.64, 1.28, 1.92,  
 341 and 2.56 Ni atoms/nm<sup>2</sup>. On the larger (4 × 4) surface  
 342 supercell, the coverage is 1.28 Ni atoms/nm<sup>2</sup>. For Ni<sub>4</sub>O<sub>4</sub>, the  
 343 size of the nanocluster on a (2 × 4) surface supercell will lead  
 344 to stronger periodic NiO–NiO interactions than for the smaller  
 345 NiO nanoclusters, which will influence the adsorption structure,  
 346 due to the NiO nanoclusters being essentially in close  
 347 proximity, and the effect of this on the change in the electronic  
 348 properties of NiO-modified TiO<sub>2</sub> will be discussed.

349 All structures show negative adsorption energies, ranging  
 350 from –3.18 to –6.15 eV giving an indication of a strong  
 351 interaction between the nanocluster and the surface and the  
 352 high stability of individual NiO nanoclusters adsorbed at TiO<sub>2</sub>,  
 353 which prevents aggregation of the clusters into larger structures  
 354 during postheating. For all deposited clusters, detailed  
 355 information about the geometry is presented in Table 1.

356 For NiO nanoclusters deposited on anatase, the NiO cluster  
 357 results in two new bonds with the TiO<sub>2</sub> surface with distances  
 358 of 1.75 and 1.91 Å. It is important to note that an O atom from  
 359 the anatase surface is pulled out of the surface by Ni from the  
 360 cluster by 0.26 Å that distorts the surface of TiO<sub>2</sub> anatase  
 361 (001), similar to SnO<sub>2</sub> adsorbed at anatase (001).<sup>32</sup> The same

behavior is observed for Ni<sub>2</sub>O<sub>2</sub> deposited at anatase (001),<sup>362</sup>  
 where in this case the O atom is pulled out of the surface by  
 363 0.17 Å upon bonding to Ni. The number of new bonds in  
 364 Ni<sub>2</sub>O<sub>2</sub> deposited on TiO<sub>2</sub> anatase (001) is three. The Ni<sub>3</sub>O<sub>3</sub>  
 365 cluster presents 11 new bonds when deposited on TiO<sub>2</sub> anatase  
 366 (001). There are five bonds between Ni and O atoms in the  
 367 range 1.93–2.20 Å while oxygen atoms from the cluster bond  
 368 to Ti surface atoms with two bonds that are 1.90 Å long. The  
 369 Ni<sub>4</sub>O<sub>4</sub> cluster deposited on TiO<sub>2</sub> anatase (001) shows six new  
 370 bonds. In this case, the surface O atom is pulled out of the  
 371 surface by 0.19 Å. Within the Ni–O nanoclusters, the Ni–O  
 372 distances are notably shorter compared to bulk NiO, for  
 373 example, 1.95 Å in Ni<sub>4</sub>O<sub>4</sub>, compared to 2.10 Å in bulk NiO. Of  
 374 the NiO nanoclusters adsorbed at anatase (001), only the  
 375 Ni<sub>3</sub>O<sub>3</sub> nanocluster shows intermetallic Ni–Ti bonds, with Ni–  
 376 Ti distances in the range 2.71–2.87 Å, which is consistent with  
 377 those in the intermetallic NiTi alloy.<sup>61</sup>  
 378

At the TiO<sub>2</sub> rutile (110) surface, the NiO cluster bonds to  
 379 the surface with six new bonds. The Ni atom from the cluster  
 380 bonds with two bridging O atoms and one surface O atom, and  
 381 the fourth metal–oxygen bond is from an O cluster atom that  
 382 bonds to Ti surface atoms. The Ni<sub>2</sub>O<sub>2</sub> cluster binds to the  
 383 surface with nine new bonds. Five metal–oxygen bonds are  
 384 from Ni cluster atoms to surface oxygen, and the last two are  
 385 from cluster oxygen to surface Ti. Ni<sub>3</sub>O<sub>3</sub> deposition on rutile  
 386 (110) results in formation of seven new bonds between the  
 387

**Table 1. Surface–Cluster Ni–O Bond Distances for NiO Clusters Adsorbed at the TiO<sub>2</sub> Anatase (001) and Rutile (110) Surfaces<sup>a</sup>**

	distance (Å)					
	anatase			rutile		
	Ni <sub>c</sub> –O <sub>s</sub>	O <sub>c</sub> –Ti <sub>s</sub>	Ni <sub>c</sub> –Ti <sub>s</sub>	Ni <sub>c</sub> –O <sub>s</sub>	O <sub>c</sub> –Ti <sub>s</sub>	Ni <sub>c</sub> –Ti <sub>s</sub>
NiO	1.75 (1)	1.91		2.08 (1)	1.80	2.61 (1)
				1.96 (1)		2.81 (1)
				2.03 (1)		
Ni <sub>2</sub> O <sub>2</sub>	1.73 (2)	1.99		2.10 (1)	1.96	2.79 (1)
		2.22		1.92 (1)	1.78	2.70 (1)
				2.09 (1)		2.58 (2)
				2.02 (2)		
				2.03 (2)		
Ni <sub>3</sub> O <sub>3</sub>	1.95 (1)	1.90	2.87 (1)	1.97 (1)	1.89	2.73 (3)
	1.93 (2)	1.90	2.85 (2)	1.96 (2)	1.89	2.87 (3)
	2.07 (3)		2.71 (3)	2.20 (3)		2.87 (3)
	2.02 (3)		2.71 (3)	2.20 (3)		
	2.20 (3)			2.05 (3)		
Ni <sub>4</sub> O <sub>4</sub>	1.95 (1)	1.93		2.21 (1)	1.89	2.74 (1)
	1.92 (2)	1.92		2.22 (1)	1.90	
	1.95 (3)			2.04 (1)		
	1.95 (4)			1.96 (2)		
			1.99 (4)			

<sup>a</sup>The numbers in parentheses are the atom numbers of Ni in each NiO nanocluster.

cluster and surface. Five bonds are between Ni cluster atoms and surface O atoms with the bond distances from 1.96 to 2.20 Å. The other two bonds come from O cluster atoms and Ti surface atoms, and their distance is 1.89 Å. The Ni<sub>4</sub>O<sub>4</sub> cluster bonds to the rutile surface with eight new bonds where three of the cluster Ni atoms create four Ni–O bonds with bridging surface O atoms and one surface O atom, with the shortest distance being 1.96 Å and the longest distance being 2.22 Å. The other two bonds are from cluster O binding with surface Ti. In each of these structures, surface Ti atoms are pulled out of the surface after bonding to cluster oxygen. For the example of NiO adsorbed at rutile (110), this Ti is displaced by 0.48 Å. At the (110) surface, we also observe the formation of new intermetallic Ni–Ti bonds between cluster Ni and surface Ti, with the distances given in Table 1. The Ni–Ti distances we observe are consistent with those in the intermetallic NiTi alloy.<sup>61</sup> Since the adsorption energies of NiO nanoclusters on the rutile (110) surface are more negative compared to those on anatase (001) for a given NiO cluster, we suggest that the presence of the new Ni–Ti bonds plays a role in further stabilization of the heterostructure. The exception is the Ni<sub>3</sub>O<sub>3</sub> nanocluster, where Ni–Ti bonds are formed at both TiO<sub>2</sub> surfaces and the adsorption energies are very similar.

Figure 6 shows the electronic density of states projected (PEDOS) on Ni 3d and Ti 3d states for NiO, Ni<sub>3</sub>O<sub>3</sub>, Ni<sub>2</sub>O<sub>2</sub>, and Ni<sub>4</sub>O<sub>4</sub> clusters adsorbed on anatase (001) (Figure 6a–d) and rutile (110) (Figure 6e–h). PEDOS plots for the O 2p states are shown in the Supporting Information (Figure S1); the Ni 3d states lie near the top of the VB in the clusters and are important in this analysis. The DOS of the clean rutile and anatase TiO<sub>2</sub> surfaces (see the Supporting Information) show the well-known O 2p derived VB, with a Ti 3d contribution, while the conduction band is dominated by the Ti 3d states in both anatase and rutile.

Examination of the PEDOS shows clearly that, upon modification of TiO<sub>2</sub> with NiO nanoclusters, NiO cluster derived states are found laying above the top of the VB edge of the rutile and anatase surfaces, which pushes the VB edge of the composite system to higher energy compared to the bare surfaces. The conduction band of the NiO-modified surfaces can show some dependence on the crystal form of TiO<sub>2</sub>. For modified rutile (110), the bottom of the conduction band is dominated by surface Ti 3d states. Interestingly, this is in contrast to the SnO<sub>2</sub>/rutile TiO<sub>2</sub> system, where the DOS near the conduction band minimum increases, with the VB unmodified.<sup>32</sup> A close inspection of the conduction band states for anatase indicates that, in some cases, for example, Ni<sub>2</sub>O<sub>2</sub>, empty NiO cluster levels are generated near the conduction band minimum.

In the NiO/TiO<sub>2</sub> system, the shift of the VB to higher energy has the consequence that the overall band gap of the composite is reduced compared to unmodified TiO<sub>2</sub>. We find in the DFT calculations a maximum band gap reduction of 0.8 eV (for Ni<sub>4</sub>O<sub>4</sub> at anatase (001)) compared to the unmodified anatase surface, and this shift is qualitatively comparable to the value determined by the VB-XPS, in Figure 4B. This can further be compared with SnO<sub>2</sub>/TiO<sub>2</sub>, where anatase modification leads to no band gap change, but rutile modification can reduce the band gap.<sup>32</sup> The narrowing of the band gap will induce visible-light absorption in the composite as shown in Figure 3. Thus, upon modification with NiO nanoclusters, NiO states appear above the VB edge of the TiO<sub>2</sub> surface, which pushes the VB up in energy. There is a case in Figure 6, where the Ni<sub>2</sub>O<sub>2</sub> nanocluster on anatase appears to also show some empty NiO states just below the anatase conduction band. In general, we can conclude that the NiO modification of TiO<sub>2</sub> will reduce the energy gap by pushing the VB edge up in energy.

We show in Figure 7 the atomic structure and PEDOS of a Ni<sub>4</sub>O<sub>4</sub> nanocluster relaxed on the rutile (110) surface with a (4 × 4) surface supercell, which has a coverage of 1.28 Ni atoms/nm<sup>2</sup> and an adsorption energy of –4.50 eV. In this case, although the effect of the smaller coverage of NiO at the surface on the final adsorption structure of the nanocluster at this surface is clear compared to Figure 5f, namely, that the Ni<sub>4</sub>O<sub>4</sub> cluster takes a different adsorption structure, the PEDOS shows that the impact of modifying TiO<sub>2</sub> with NiO is unchanged, namely, that there are NiO-derived states found at the top of the VB, which will reduce the energy gap compared to unmodified TiO<sub>2</sub>.

The oxidation state of the metal oxide surface modifier can also affect the photocatalytic activity of TiO<sub>2</sub>.<sup>33</sup> A Bader charge analysis<sup>62</sup> on Ni for the NiO nanoclusters deposited on both surfaces gives net charges on Ni ranging from 8.7 to 8.9 electrons, which are consistent with a Ni<sup>2+</sup> oxidation state. Moreover, in TiO<sub>2</sub>, the computed net Bader charges are approximately +1.3 electrons, which is typical for the Ti<sup>4+</sup> oxidation state. The oxidation states of Ni and Ti are in agreement with those determined by XPS.<sup>37</sup>

On the basis of these results above, the NiO surface modification effect on the photocatalytic activity of P-25 can be rationalized as follows and indicated in Figure 8. NiO clusters possess a strong interaction with the anatase and rutile surfaces through Ni–O–Ti bonds for anatase and rutile and additional Ni–Ti bonds for rutile. As a result of the mixing of the Ni 3d levels, the VB maximum of TiO<sub>2</sub> rises significantly, while new vacant levels are generated near the conduction band minimum of anatase that is the major phase of P-25.

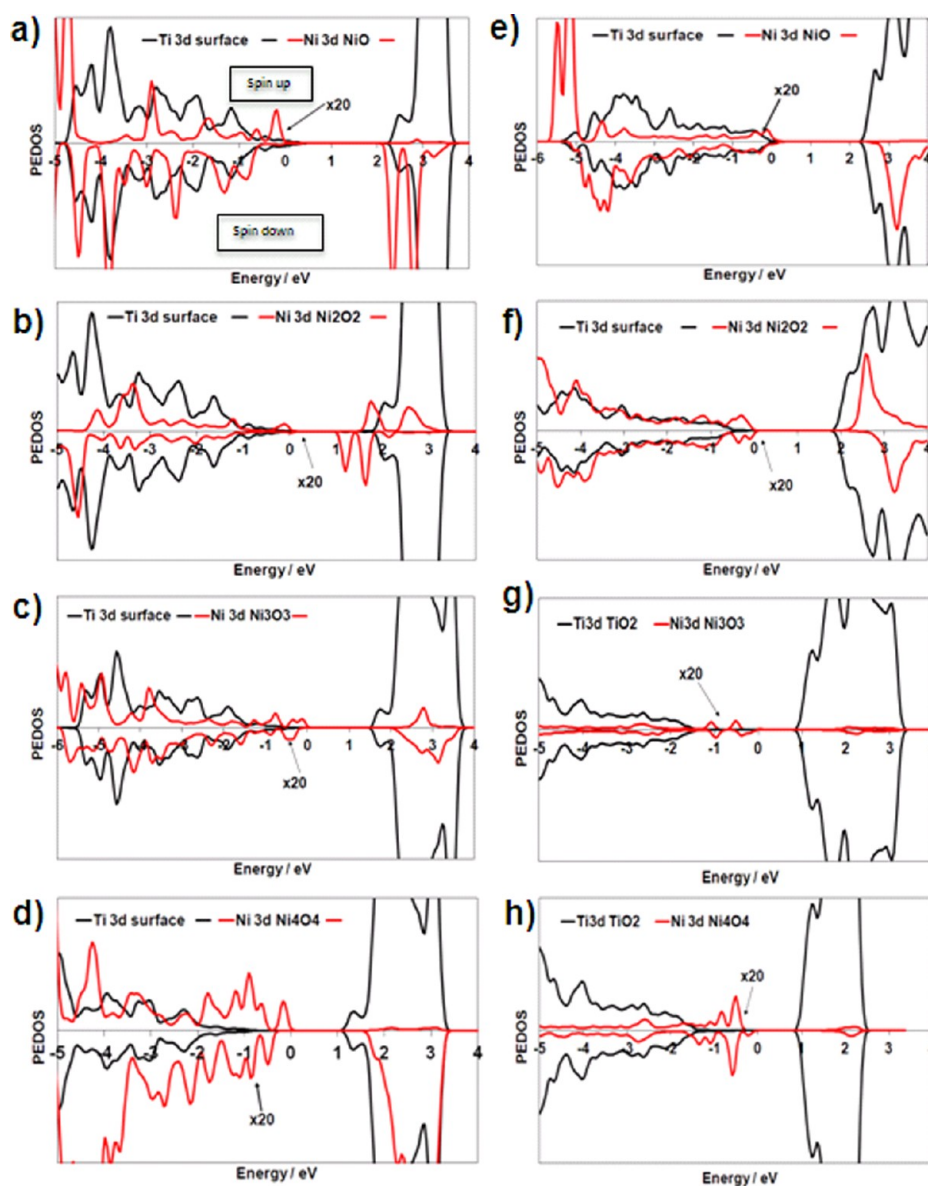


**Figure 6.** Spin polarized PEDOS on Ni 3d and Ti3d states for (a) NiO, (b) Ni<sub>2</sub>O<sub>2</sub>, (c) Ni<sub>3</sub>O<sub>3</sub>, and (d) Ni<sub>4</sub>O<sub>4</sub> clusters supported on the anatase (001) surface and for (e) NiO, (f) Ni<sub>2</sub>O<sub>2</sub>, (g) Ni<sub>3</sub>O<sub>3</sub>, and (h) Ni<sub>4</sub>O<sub>4</sub> clusters supported on the TiO<sub>2</sub> rutile (110) surface.

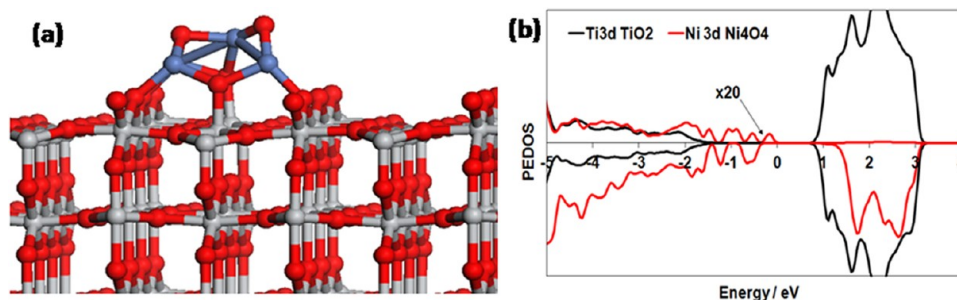


**Figure 7.** (a) Atomic structure and (b) PEDOS for a Ni<sub>4</sub>O<sub>4</sub> cluster adsorbed at the rutile (110) surface in a (4 × 4) surface supercell.

485 Upon visible-light irradiation of NiO/P-25, the electrons in  
 486 the surface Ni 3d sub-band are excited to the TiO<sub>2</sub> conduction  
 487 band. This surface-to-bulk interfacial electron transfer (IET)  
 488 enhances the charge carrier separation. The holes generated at  
 489 the surface d sub-band oxidize adsorbed 2-naphthol and *p*-  
 490 cresol. On the other hand, the electrons in the TiO<sub>2</sub> conduction

band are consumed by O<sub>2</sub> reduction. This process can be the  
 491 key to increasing photocatalytic activity in the oxidative  
 492 decomposition of organic pollutants.<sup>63,64</sup> Figure 8 suggests  
 493 that the excited electrons in the anatase conduction band can  
 494 be transferred to the surface levels of the NiO species, which  
 495 further assists the electron transfer to O<sub>2</sub> as previously  
 496



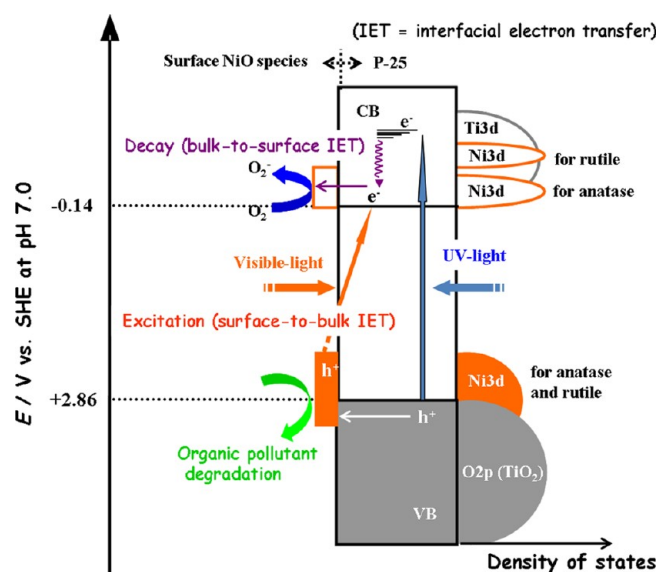


Figure 8. Energy band diagram for NiO-modified TiO<sub>2</sub>.

497 confirmed by the electrochemical experiments.<sup>37</sup> This action  
 498 mechanism of the NiO clusters should also operate under UV-  
 499 light irradiation. Consequently, the NiO surface modified P-25  
 500 causes the high activities under illumination of visible light and  
 501 UV light. A final point is that, in the experiments, an optimum  
 502 Ni loading for photocatalytic activity is found (Figure 2A,B),  
 503 although above this loading, the NiO–TiO<sub>2</sub> system displays a  
 504 continuous decrease in the band gap. With the results of this  
 505 work showing that the increased loading of NiO results in a rise  
 506 in the VB edge of the composite system compared to  
 507 unmodified TiO<sub>2</sub>, we can explain this finding as follows. The  
 508 low VB edge in unmodified TiO<sub>2</sub> imparts good oxidative power  
 509 to the holes formed after light excitation, while an upward shift  
 510 of the VB edge will weaken the oxidation power of the holes.  
 511 Thus, with an increase in NiO loading, the VB edge is shifted  
 512 upward (Figures 3, 4, and 6), which therefore weakens the  
 513 oxidative power of the holes and results in an optimal loading  
 514 of NiO on TiO<sub>2</sub>. A similar result has been found for other metal  
 515 oxide nanocluster modified TiO<sub>2</sub>,<sup>30–33</sup> indicating that this  
 516 phenomenon is quite general; that is, there will be an optimum  
 517 loading of a second metal oxide on TiO<sub>2</sub> that shifts the VB edge  
 518 such that visible-light absorption is realized but that the  
 519 oxidative power of the photoexcited holes is not reduced too  
 520 much.

#### 4. CONCLUSIONS

521 We have shown that the surface modification of P-25 (anatase/  
 522 rutile = 4:1 w/w) with NiO clusters gives rise to high visible-  
 523 light activities for 2-naphthol and *p*-cresol concomitantly with  
 524 significant increases in the UV-light activities. We have  
 525 presented DFT simulations of nickel oxide clusters adsorbed  
 526 on TiO<sub>2</sub> anatase (001) and rutile (110) surfaces to understand  
 527 the origin of visible-light activity in these heterostructures. We  
 528 find that NiO clusters are deposited on TiO<sub>2</sub> surfaces with large  
 529 adsorption energies ranging from –3.18 to –6.15 eV, with  
 530 metallic Ni–Ti bonds leading to extra stabilization on rutile  
 531 (110) compared with anatase (001). The deposited clusters  
 532 cause the narrowing of the TiO<sub>2</sub> band gap, which pushes the  
 533 photoactivity into the visible region due to the presence of NiO  
 534 states at the top of the valence band of TiO<sub>2</sub>. The present  
 535 energy level alignments enhance the charge separation and the

electron transfer to O<sub>2</sub>, which are the origins of photocatalytic  
 536 efficiency enhancement. These results are consistent with  
 537 experimental data. 538

#### ■ ASSOCIATED CONTENT

##### Supporting Information

539  
 540 Photocatalytic activities of metal oxide surface modified P-25  
 541 (Degussa) for 2-naphthol degradation; Ni 3d and O 2p PEDOS  
 542 for NiO nanocluster modified TiO<sub>2</sub>; electronic DOS for  
 543 unmodified rutile (110) and anatase (001) surfaces. This  
 544 material is available free of charge via the Internet at [http://](http://pubs.acs.org)  
 545 [pubs.acs.org](http://pubs.acs.org). 546

#### ■ AUTHOR INFORMATION

##### Corresponding Author

547  
 548 \*E-mail: [michael.nolan@tyndall.ie](mailto:michael.nolan@tyndall.ie) (M.N.); [h-tada@apch.](mailto:h-tada@apch.kindai.ac.jp)  
 549 [kindai.ac.jp](mailto:kindai.ac.jp) (H.T.). 550

##### Notes

551  
 552 The authors declare no competing financial interest. 552

#### ■ ACKNOWLEDGMENTS

553  
 554 M.N. and A.I. acknowledge support from Science Foundation  
 555 Ireland (SFI) through the Starting Investigator Research Grant  
 556 Program, project “EMOIN”, grant number SFI 09/SIRG/  
 557 I1620, and computing resources at Tyndall provided by SFI  
 558 and by the SFI and Higher Education Authority funded Irish  
 559 Centre for High End Computing. We acknowledge support  
 560 from the European Union through the COST Action CM1104  
 561 “Reducible Oxide Chemistry, Structure and Functions”. H.T.  
 562 acknowledges supports from the Ministry of Education,  
 563 Science, Sport, and Culture, Japan through a Grant-in-Aid for  
 564 Scientific Research (C) no. 24550239, and Nippon Sheet Glass  
 565 Foundation for Materials Science and Engineering, and by  
 566 Sumitomo Foundation. 566

#### ■ REFERENCES

- 567  
 568 (1) Nie, X. L.; Zhou, S. P.; Maeng, G.; Sohlberg, K. Doping of TiO<sub>2</sub>  
 569 Polymorphs for Altered Optical and Photocatalytic Properties. *Int. J.*  
 570 *Photoenergy* **2009**, No. 294042. 570  
 571 (2) Nowotny, J. Titanium Dioxide-Based Semiconductors for Solar-  
 572 Driven Environmentally Friendly Applications: Impact of Point  
 573 Defects on Performance. *Energy Environ. Sci.* **2008**, *1*, 556–572. 573  
 574 (3) Asahi, R.; Morikawa, T.; Ohwaki, K.; Aoki, K.; Taga, Y. Visible-  
 575 Light Photocatalysis in Nitrogen-Doped Titanium Oxides. *Science*  
 576 **2001**, *293*, 269–271. 576  
 577 (4) Di Valentin, C.; Finazzi, E.; Pacchioni, G.; Selloni, A.; Livraghi, S.;  
 578 Paganini, M. C.; Giamello, E. N-Doped TiO<sub>2</sub>: Theory and Experiment. *577*  
 579 *Chem. Phys.* **2007**, *339*, 44–56. 579  
 580 (5) Di Valentin, C.; Pacchioni, G.; Selloni, A. Origin of the Different  
 581 Photoactivity of N-Doped Anatase and Rutile TiO<sub>2</sub>. *Phys. Rev. B* **2004**,  
 582 *70*, 085116/1–085116/4. 582  
 583 (6) Barolo, G.; Livraghi, S.; Chiesa, M.; Paganini, M. C.; Giamello,  
 584 E. Mechanism of the Photoactivity under Visible Light of N-Doped  
 585 Titanium Dioxide. Charge Carriers Migration in Irradiated N-TiO<sub>2</sub>  
 586 Investigated by Electron Paramagnetic Resonance. *J. Phys. Chem. C*  
 587 **2012**, *116*, 20887–20894. 587  
 588 (7) Ceotto, M.; Lo Presti, L.; Cappelletti, G.; Meroni, D.;  
 589 Spadavecchia, F.; Zecca, R.; Leoni, M.; Scardi, P.; Bianchi, C. L.;  
 590 Ardizzone, S. About the Nitrogen Location in Nanocrystalline N-  
 591 Doped TiO<sub>2</sub>: Combined DFT and EXAFS Approach. *J. Phys. Chem. C*  
 592 **2012**, *116*, 1764–1771. 592  
 593 (8) Wu, G.; Nishikawa, T.; Ohtani, B.; Chen, A. Synthesis and  
 594 Characterization of Carbon-Doped TiO<sub>2</sub> Nanostructures with  
 595 Enhanced Visible Light Response. *Chem. Mater.* **2007**, *19*, 4530–4537. 595

- (9) Park, J. H.; Kim, S.; Bard, A. J. Novel Carbon-Doped TiO<sub>2</sub> Nanotube Arrays with High Aspect Ratios for Efficient Solar Water Splitting. *Nano Lett.* **2006**, *6*, 24–28.
- (10) Di Valentin, C.; Pacchioni, G.; Selloni, A. Theory of Carbon Doping of Titanium Dioxide. *Chem. Mater.* **2005**, *17*, 6656–6665.
- (11) Graciani, J.; Ortega, Y.; Sanz, J. F. Carbon Doping of the TiO<sub>2</sub> (110) Rutile Surface. A Theoretical Study Based on DFT. *Chem. Mater.* **2009**, *21*, 1431–1438.
- (12) Wang, H.; Lewis, J. P. Second-Generation Photocatalytic Materials: Anion-Doped TiO<sub>2</sub>. *J. Phys.: Condens. Matter* **2006**, *18*, 421–434.
- (13) Wang, H.; Lewis, J. P. Effects of Dopant States on Photoactivity in Carbon-Doped TiO<sub>2</sub>. *J. Phys.: Condens. Matter* **2005**, *17*, L209–L214.
- (14) Di Valentin, C.; Pacchioni, G.; Onishi, H.; Kudo, A. Cr/Sb Co-Doped TiO<sub>2</sub> from First Principles Calculations. *Chem. Phys. Lett.* **2009**, *469*, 166–171.
- (15) Yu, J. G.; Xiang, Q. J.; Zhou, M. H. Preparation, Characterization and Visible-Light-Driven Photocatalytic Activity of Fe-Doped Titania Nanorods and First-Principles Study for Electronic Structures. *Appl. Catal., B* **2009**, *90*, 595–602.
- (16) Long, R.; English, N. J. First-Principles Calculation of Synergistic (N, P)-Codoping Effects on the Visible-Light Photocatalytic Activity of Anatase TiO<sub>2</sub>. *J. Phys. Chem. C* **2010**, *114*, 11984–11990.
- (17) Zheng, J. W.; Bhattacharayya, A.; Wu, P.; Chen, Z.; Highfield, J.; Dong, Z. L.; Xu, R. The Origin of Visible Light Absorption in Chalcogen Element (S, Se, and Te)-Doped Anatase TiO<sub>2</sub> Photocatalysts. *J. Phys. Chem. C* **2010**, *114*, 7063–7069.
- (18) Peng, H. W.; Li, J. B.; Li, S. S.; Xia, J. B. First-Principles Study of the Electronic Structures and Magnetic Properties of 3d Transition Metal-Doped Anatase TiO<sub>2</sub>. *J. Phys.: Condens. Matter* **2008**, *20*, 125207.
- (19) Bian, L.; Song, M. X.; Zhou, T. L.; Zhao, X. Y.; Dai, Q. Q. Band Gap Calculation and Photo Catalytic Activity of Rare Earths Doped Rutile TiO<sub>2</sub>. *J. Rare Earths* **2009**, *27*, 461–468.
- (20) Kubacka, A.; Fernandez-Garcia, M.; Colon, G. Advanced Nanoarchitectures for Solar Photocatalytic Applications. *Chem. Rev.* **2012**, *112*, 1555–1614.
- (21) Primo, A.; Corma, A.; Garcia, H. Titania Supported Gold Nanoparticles as Photocatalyst. *Phys. Chem. Chem. Phys.* **2011**, *13*, 886–910.
- (22) Herrmann, J. M. Detrimental Cationic Doping of Titania in Photocatalysis: Why Chromium Cr<sup>3+</sup>-Doping is a Catastrophe for Photocatalysis, Both under UV- and Visible Irradiations. *New. J. Chem.* **2012**, *36*, 883–890.
- (23) Tada, H.; Mitsui, T.; Kiyonaga, T.; Akita, T.; Tanaka, K. All-Solid-State Z-Scheme in CdS–Au–TiO<sub>2</sub> Three-Component Heterojunction System. *Nat. Mater.* **2006**, *5*, 782–786.
- (24) Williams, G.; Seger, B.; Kamat, P. V. TiO<sub>2</sub>-Graphene Nanocomposites. UV-Assisted Photocatalytic Reduction of Graphene Oxide. *ACS Nano* **2008**, *2*, 1487–1491.
- (25) Murakami, N.; Chiyoya, T.; Tsubota, T.; Ohno, T. Switching Redox Site of Photocatalytic Reaction on Titanium(IV) Oxide Particles Modified with Transition-Metal Ion Controlled by Irradiation Wavelength. *Appl. Catal., A* **2008**, *348*, 148–152.
- (26) Yu, H.; Irie, H.; Shimodaira, Y.; Hosogi, Y.; Kuroda, Y.; Miyauchi, M.; Hashimoto, K. An Efficient Visible-Light-Sensitive Fe(III)-Grafted TiO<sub>2</sub> Photocatalyst. *J. Phys. Chem. C* **2010**, *114*, 16481–16487.
- (27) Hong, S. J.; Lee, S.; Jang, J. S.; Lee, J. S. Heterojunction BiVO<sub>4</sub>/WO<sub>3</sub> Electrodes for Enhanced Photoactivity of Water Oxidation. *Energy Environ. Sci.* **2011**, *4*, 1781–1787.
- (28) Kong, L.; Jiang, Z.; Xiao, T.; Lu, L.; Jones, M. O.; Edwards, P. P. Exceptional Visible-Light-Driven Photocatalytic Activity over BiOBr–ZnFe<sub>2</sub>O<sub>4</sub> Heterojunctions. *Chem. Commun.* **2011**, *47*, 5512–5514.
- (29) Libera, J. A.; Elam, J. W.; Sather, N. F.; Rajh, T. M.; Dimitrijevic, N. M. Iron(III)-Oxo Centers on TiO<sub>2</sub> for Visible-Light Photocatalysis. *Chem. Mater.* **2010**, *22*, 409–413.
- (30) Tada, H.; Jin, Q.; Nishijima, H.; Yamamoto, H.; Fujishima, M.; Okuoka, S.-i.; Hattori, T.; Sumida, Y.; Kobayashi, H. Titanium(IV) Dioxide Surface-Modified with Iron Oxide as a Visible Light Photocatalyst. *Angew. Chem., Int. Ed.* **2011**, *50*, 3501–3505.
- (31) Jin, Q.; Fujishima, M.; Tada, H. Visible-Light-Active Iron Oxide-Modified Anatase Titanium(IV) Dioxide. *J. Phys. Chem. C* **2011**, *115*, 6478–6483.
- (32) Fujishima, M.; Jin, Q.; Yamamoto, H.; Tada, H.; Nolan, M. Tin Oxide-Surface Modified Anatase Titanium(IV) Dioxide with Enhanced UV-Light Photocatalytic Activity. *Phys. Chem. Chem. Phys.* **2012**, *14*, 705–711.
- (33) Jin, Q.; Fujishima, M.; Nolan, M.; Iwaszuk, A.; Tada, H. Photocatalytic Activities of Tin(IV) Oxide Surface-Modified Titanium(IV) Dioxide Show a Strong Sensitivity to the TiO<sub>2</sub> Crystal Form. *J. Phys. Chem. C* **2012**, *116*, 12621–12626.
- (34) Boppana, V. B. R.; Lobo, R. F. SnO<sub>x</sub>-ZnGa<sub>2</sub>O<sub>4</sub> Photocatalysts with Enhanced Visible Light Activity. *ACS Catal.* **2011**, *1*, 923–928.
- (35) Cheng, H.; Huang, B.; Dai, Y.; Qin, X.; Zhang, X. One-Step Synthesis of the Nanostructured AgI/BiOI Composites with Highly Enhanced Visible-Light Photocatalytic Performances. *Langmuir* **2010**, *26*, 6618–6624.
- (36) Murakami, N.; Chiyoya, T.; Tsubota, T.; Ohno, T. Switching Redox Site of Photocatalytic Reaction on Titanium(IV) Oxide Particles Modified with Transition-Metal Ion Controlled by Irradiation Wavelength. *Appl. Catal., A* **2008**, *348*, 148–152.
- (37) Jin, Q.; Ikeda, T.; Fujishima, M.; Tada, H. Nickel(II) Oxide Surface-Modified Titanium(IV) Dioxide as a Visible-Light-Active Photocatalyst. *Chem. Commun.* **2011**, *47*, 8814–8816.
- (38) Iwaszuk, A.; Nolan, M. Reactivity of Sub 1 nm Supported Clusters: (TiO<sub>2</sub>)<sub>n</sub> Clusters Supported on Rutile TiO<sub>2</sub> (110). *Phys. Chem. Chem. Phys.* **2011**, *13*, 4963–4973.
- (39) Nolan, M. Surface Modification of TiO<sub>2</sub> with Metal Oxide Nanoclusters: a Route to Composite Photocatalytic Materials. *Chem. Commun.* **2011**, *47*, 8617–8619.
- (40) Kresse, G.; Hafner, J. Ab Initio Molecular-Dynamics Simulation of the Liquid-Metal-Amorphous-Semiconductor Transition in Germanium. *Phys. Rev. B* **1994**, *49*, 14251–14269.
- (41) Blöchl, P. E. Projector Augmented-Wave Method. *Phys. Rev. B* **1994**, *50*, 17953–17979.
- (42) Perdew, J. P. In *Electronic Structure of Solids '91*; Ziesche, P., Eschrig, H., Eds.; Akademie Verlag: Berlin, Germany, 1991.
- (43) Diebold, U. The Surface Science of Titanium Dioxide. *Surf. Sci. Rep.* **2003**, *48*, 53–229.
- (44) Liu, M.; Piao, L.; Zhao, L.; Ju, S.; Yan, Z.; He, T.; Zhou, C.; Wang, W. Anatase TiO<sub>2</sub> Single Crystals with Exposed {001} and {110} Facets: Facile Synthesis and Enhanced Photocatalysis. *Chem. Commun.* **2010**, *46*, 1664–1666.
- (45) Yang, W.; Li, J.; Wang, Y.; Zhu, F.; Shi, W.; Wan, F.; Xu, D. A Facile Synthesis of Anatase TiO<sub>2</sub> Nanosheets-Based Hierarchical Spheres with over 90% {001} Facets for Dye-Sensitized Solar Cells. *Chem. Commun.* **2011**, *47*, 1809–1811.
- (46) Anisimov, V. I.; Zaanen, J.; Andersen, O. K. Band Theory and Mott Insulators: Hubbard U instead of Stoner I. *Phys. Rev. B* **1991**, *44*, 943–954.
- (47) Dudarev, S. L.; Botton, G. A.; Savrasov, S. Y.; Humphreys, C. J.; Sutton, A. P. Electron-Energy-Loss Spectra and the Structural Stability of Nickel Oxide: An LSDA+U Study. *Phys. Rev. B* **1998**, *57*, 1505–1509.
- (48) Morgan, B. J.; Watson, G. W. A DFT+U Description of Oxygen Vacancies at the TiO<sub>2</sub> Rutile (110) Surface. *Surf. Sci.* **2007**, *601*, 5034–5041.
- (49) Ganduglia-Pirovano, M. V.; Hofmann, A.; Sauer, J. Oxygen Vacancies in Transition Metal and Rare Earth Oxides: Current State of Understanding and Remaining Challenges. *Surf. Sci. Rep.* **2007**, *62*, 219–270.
- (50) Nolan, M.; Grigoleit, S.; Sayle, D. C.; Parker, S. C.; Watson, G. W. Density Functional Theory Studies of the Structure and Electronic Structure of Pure and Defective Low Index Surfaces of Ceria. *Surf. Sci.* **2005**, *576*, 217–229.

- 734 (51) Ferrari, A. M.; Pisani, C.; Cincini, F.; Giordano, L.; Pacchioni,  
735 G. Cationic and Anionic Vacancies on the NiO(100) Surface: DFT+U  
736 and Hybrid Functional Density Functional Theory Calculations. *J.*  
737 *Chem. Phys.* **2007**, *127*, 174711.
- 738 (52) Long, R.; English, N. J.; Mooney, D. A. Electronic Structures of  
739 N- and C-Doped NiO from First-Principles Calculations. *Phys. Lett. A*  
740 **2010**, *374*, 1184–1187.
- 741 (53) Yu, N.; Zhang, W.-B.; Wang, N.; Wang, W.-F.; Tang, B.-Y.  
742 Water Adsorption on a NiO(100) Surface: A GGA+U Study. *J. Phys.*  
743 *Chem. C* **2008**, *112*, 452–457.
- 744 (54) Tada, H.; Matsui, H.; Shiota, F.; Nomura, M.; Ito, S.; Yoshihara,  
745 M.; Esumi, K. Heterosupramolecular Photocatalysis: Oxidation of  
746 Organic Compounds in Nanospaces between Surfactant Bilayers  
747 Formed on TiO<sub>2</sub>. *Chem. Commun.* **2002**, 1678–1679.
- 748 (55) Nolan, M.; Iwaszuk, A.; Tada, H. Molecular Metal Oxide  
749 Cluster-Surface Modified Titanium(IV) Dioxide Photocatalysts. *Aust.*  
750 *J. Chem.* **2012**, *65*, 624–632.
- 751 (56) Niishiro, R.; Kato, H.; Kudo, A. Nickel and Either Tantalum or  
752 Niobium-Codoped TiO<sub>2</sub> and SrTiO<sub>3</sub> Photocatalysts with Visible-Light  
753 Response for H<sub>2</sub> or O<sub>2</sub> Evolution from Aqueous Solutions. *Phys. Chem.*  
754 *Chem. Phys.* **2005**, *7*, 2241–2245.
- 755 (57) Liu, G.; Wang, L.; Yang, H. G.; Cheng, H. -M.; Lu, G. Q.  
756 Titania-Based Photocatalysts—Crystal Growth, Doping and Hetero-  
757 structuring. *J. Mater. Chem.* **2010**, *20*, 831–843.
- 758 (58) Serpone, N.; Lawless, D.; Khairutdinov, R. Size Effects on the  
759 Photophysical Properties of Colloidal Anatase TiO<sub>2</sub> Particles: Size  
760 Quantization versus Direct Transitions in This Indirect Semi-  
761 conductor. *J. Phys. Chem.* **1995**, *99*, 16646–16654.
- 762 (59) Anpo, M.; Takeuchi, M. The Design and Development of  
763 Highly Reactive Titanium Oxide Photocatalysts Operating under  
764 Visible Light Irradiation. *J. Catal.* **2003**, *216*, 505–516.
- 765 (60) Kitano, M.; Funatsu, K.; Matsuoka, M.; Ueshima, M.; Anpo, M.  
766 Preparation of Nitrogen-Substituted TiO<sub>2</sub> Thin Film Photocatalysts by  
767 the Radio Frequency Magnetron Sputtering Deposition Method and  
768 Their Photocatalytic Reactivity under Visible Light Irradiation. *J. Phys.*  
769 *Chem. B* **2006**, *110*, 25266–25272.
- 770 (61) Nolan, M.; Tofail, S. A. M. Density Functional Theory  
771 Simulation of Titanium Migration and Reaction with Oxygen in the  
772 Early Stages of Oxidation of Equiatomic NiTi alloy. *Biomaterials* **2010**,  
773 *31*, 3439–3448.
- 774 (62) Henkelman, G.; Arnaldsson, A.; Jónsson, H. A Fast and Robust  
775 Algorithm for Bader Decomposition of Charge Density. *Comput.*  
776 *Mater. Sci.* **2006**, *36*, 354–360.
- 777 (63) Wang, C. M.; Heller, A.; Gerischer, H. Palladium Catalysis of O<sub>2</sub>  
778 Reduction by Electrons Accumulated on TiO<sub>2</sub> Particles during  
779 Photoassisted Oxidation of Organic Compounds. *J. Am. Chem. Soc.*  
780 **1992**, *114*, 5230–5234.
- 781 (64) Hoffmann, M. R.; Martin, S. T.; Choi, W.; Bahnemann, D. W.  
782 Environmental Application of Semiconductor Photocatalysis. *Chem.*  
783 *Rev.* **1995**, *95*, 69–96.